#### **Research Article**

Yuto Shimizu and Takahiro Nomura\*

# Al-Si-Fe alloy-based phase change material for high-temperature thermal energy storage

https://doi.org/10.1515/htmp-2022-0280 received January 05, 2023; accepted June 06, 2023

Abstract: Carnot batteries, a type of power-to-heat-topower energy storage, are in high demand as they can provide a stable supply of renewable energy. Latent heat storage (LHS) using alloy-based phase change materials (PCMs), which have high heat storage density and thermal conductivity, is a promising method. However, LHS requires the development of a PCM with a melting point suitable for its application. For the Carnot battery, the reuse of a conventional ultra-supercritical coal-fired power plant with a maximum operating temperature of approximately 650°C is considered. Therefore, developing a 600°C-class alloy-based PCM is crucial for realizing a highly efficient and environmentally friendly Carnot battery. Using thermodynamic calculation software (FactSage), we found that Al-5.9 mass% Si-1.6 mass% Fe undergoes a phase transformation at 576-619°C, a potential 600°C-class PCM. In this study, we investigated the practicality of an Al-Si-Fe PCM as an LHS material based on its heat storage and release properties and form stability. The examined Al-Si-Fe PCM melted until approximately 620°C with a latent heat capacity of 375–394 J·g<sup>-1</sup>. Furthermore, the PCM was found to have a thermal conductivity of approximately 160 W⋅m<sup>-1</sup>⋅K<sup>-1</sup> in the temperature range of 100–500°C, which is significantly better than that of conventional sensible heat storage materials in terms of heat storage capacity and thermal conductivity.

**Keywords:** thermal energy storage, latent heat storage, phase change material, aluminum alloy, Carnot battery

**Yuto Shimizu:** Graduate School of Engineering, Hokkaido University, Kita 13 Nishi 8, Kita-ku, Sapporo, 060-8628, Japan

### 1 Introduction

Renewable energy is desired as the main source of electricity to realize a decarbonized society. However, variability and intermittency have been identified as the drawbacks of renewable energy [1]. Consequently, introducing large-scale energy storage in the power grid ensures a steady energy supply. Thermal energy storage (TES) is an attractive technology owing to its advantages, such as low cost, long lifetime, no geographical restrictions, and suitability for long-term energy storage [2,3].

Carnot batteries, a power-to-heat-to-power system that uses TES as an energy storage process, are receiving increasing attraction as they can provide a stable supply of renewable energy [4,5]. Carnot battery is a system that temporarily stores renewable energy as thermal energy and generates electricity according to the demand. In particular, its development is in progress in Europe, and SIE-MENS Gamesa has already demonstrated a facility with an energy storage capacity of 130 MWh, using volcanic rocks as a TES material [6]. Many other demonstrations and studies on the applicability of Carnot batteries have been reported. Novotny et al. reviewed the Carnot battery, whose commercial development is underway [7]. One of the main aims of developing the Carnot battery is to reuse the power generation systems and infrastructure of conventional coal-fired power plants; companies such as SIE-MENS Gamesa [6], Salt X [8], and RWE Power [9] have indicated their intentions. In addition, integrating hightemperature TES into coal-fired power generation can improve the load flexibility of power generation and reduce coal consumption, as reported in a modeling study by Cao et al. [10]. Thus, the Carnot battery concept can help realize decarbonization in an environmentally friendly and economical manner by reusing conventional power generation plants.

The advancement of the Carnot battery requires developing a high-temperature TES suitable for conventional steam turbine applications. To increase the power generation efficiency of steam turbines, it is generally desirable to increase the input steam temperature to the maximum

<sup>\*</sup> Corresponding author: Takahiro Nomura, Faculty of Engineering, Hokkaido University, Kita 13 Nishi 8, Kita-ku, Sapporo, 060-8628, Japan, e-mail: nms-tropy@eng.hokudai.ac.jp, tel: +81 11 706 6842; fax: +81 11 706 6849

possible extent. Conventional coal-fired power generation in the several 100 to 1,000 MW class uses ultra-supercritical steam turbines; however, the input steam temperature is limited by the heat resistance temperature of the steel materials that compose the turbine. Consequently, the operating temperature of steam turbines has increased with the development of more suitable materials [11,12]. Ultra-supercritical steam power generation from 1950 to 2000 had an input steam temperature of 540–580°C, whereas, since 2000, most plants have operated with input steam temperatures of approximately 600-620°C [11]. The structural material mainly used in such plants is austenitic stainless steel with a heat resistance temperature of approximately 650°C [12]. Therefore, it is crucial to develop a 600°C-class TES system that can operate at temperatures up to 650°C for developing a Carnot battery, which is a reused conventional coal-fired power generation system.

The two main types of high-temperature TES are sensible heat TES (SHTES) and latent heat TES (LHTES). SHTES uses the specific heat of materials in the solid or liquid state, such as stone, concrete, or molten salt, to store heat. In particular, molten salts are widely used as commercial high-temperature SHTES materials [13,14]. Moreover, concentrated solar thermal power generation integrated with high-temperature TES with a heat storage capacity of 1,000 MWh using NaNO<sub>3</sub>-40 mass% KNO<sub>3</sub> (solar salt) has been commercialized [14,15]. However, the usual utilization temperature of solar salt is limited to 565°C, the thermal decomposition temperature [14].

LHTES is a technology that stores heat mainly using the solid-liquid phase change of phase-change materials (PCMs). PCM provides a high heat storage density, a constant temperature heat supply at the melting point  $(T_m)$ , and the ability to operate only with heat input and output. Therefore, a compact and exergy-efficient system can be designed for LHTES compared to that for SHTES. As the operating temperature of LHTES depends on the melting point of the PCM, an appropriate PCM must be selected for application [16]. For example, to design an LHTES for highefficiency, ultra-supercritical steam power generation operating at temperatures up to 650°C, a PCM that melts completely below 650°C with the highest possible melting point is particularly suitable. Generally, LHTES uses organic PCM in the low-temperature range and molten salts or metal/alloy PCM in the high-temperature range.

Molten salt and metal/alloy systems are high-temperature PCMs in the 500–650°C class [16,17]. In the molten salt system, fluoride salts (e.g., KF-60 mol% KBr:  $T_{\rm m}$  = 576°C and LiF-35 mol% NaF-13 mol% CaF $_2$ :  $T_{\rm m}$  = 615°C) and chloride salts (e.g., KCl-55 mol% KF:  $T_{\rm m}$  = 605°C and LiCl-5.5 mol%

MgF<sub>2</sub>:  $T_{\rm m}$  = 573°C), and in alloy systems, Al-based (Al-33.08 mass% Cu:  $T_{\rm m}$  = 548°C, Al-11.7 mass% Si-5.16 mass% Mg:  $T_{\rm m}$  = 555°C, Al-12 mass% Si:  $T_{\rm m}$  = 576°C) and Cu-based alloys such as Cu-46.3 mass% Al-4.6 mass% Si ( $T_{\rm m}$  = 571°C) have been reviewed by Costa and Kenisarin [17]. Alloy-based PCMs have several advantages, such as no thermal decomposition, low reactivity with other materials, tens to hundreds of times higher thermal conductivity [18], and small volume expansion during solid—liquid phase transformation [19], when compared with the molten salt systems. However, there are extremely few alloy-based PCMs that melt at approximately 600°C, and even those compositions that have been reported contain Cu and Mg, resulting in high material costs.

Therefore, we attempted to find a 600°C-class alloybased PCM that melts completely at temperatures below 650°C. Figure 1 shows the phase diagram of (a) Al-Si-Fe ternary system, (b) Al-Si-Fe ternary system on Al-rich corner, and (c) Al<sub>0.992</sub>Fe<sub>0.008</sub>-Si on Al<sub>0.992</sub>Fe<sub>0.008</sub>-rich side, which were prepared from the "Phase Diagram" module and the "SGTE 2020 alloy" database in FactSage 8.1 software. From Figure 1(a) and (c), we found that Al-5.9 mass% Si-1.6 mass% Fe melts in the temperature range of 576–619°C. Figure 2 shows the relationship between the accumulated heat storage capacity ( $\Delta H$ ) and temperature for the Al-5.9 mass% Si-1.6 mass% Fe alloy, which was prepared from the "Equilib" module and the "SGTE 2020 alloy" database in FactSage 8.1 software. As shown in Figure 2, the Al-5.9 mass% Si-1.6 mass% Fe alloy is expected to have a total latent heat  $(L_{\text{m,total}})$  of 436 J·g<sup>-1</sup>, consisting of the latent heat at the low-temperature side  $(L_{m1}:173 \text{ J}\cdot\text{g}^{-1})$  at 576°C and that at the high-temperature side ( $L_{m2}$ :317 J·g<sup>-1</sup>) between 576 and 619°C.

Al–Si–Fe PCM is promising as a 600°C-class high-temperature PCM and has many advantages in terms of cost and environmental aspects. Al–Si alloys and Fe are among the most used metallic materials, so they are inexpensive. In addition, approximately one million tons of Al is produced annually, and approximately 35% is recycled from scrap materials [20]. Furthermore, as Fe is a major impurity in Al-based products and is always present in commercial materials, it negatively affects the castability and mechanical strength of recycled Al alloys [20,21]. Therefore, Al alloys containing Fe are usually available as inexpensive scrap materials before recycling.

During the recycling of Al alloys containing 1.2% or more Fe, depending on the composition and intended use of the product, measures such as diluting the Fe concentration with high-purity Al (downcycling) [20,22], separating Al–Si–Fe intermetallic compounds by filtration [23] or

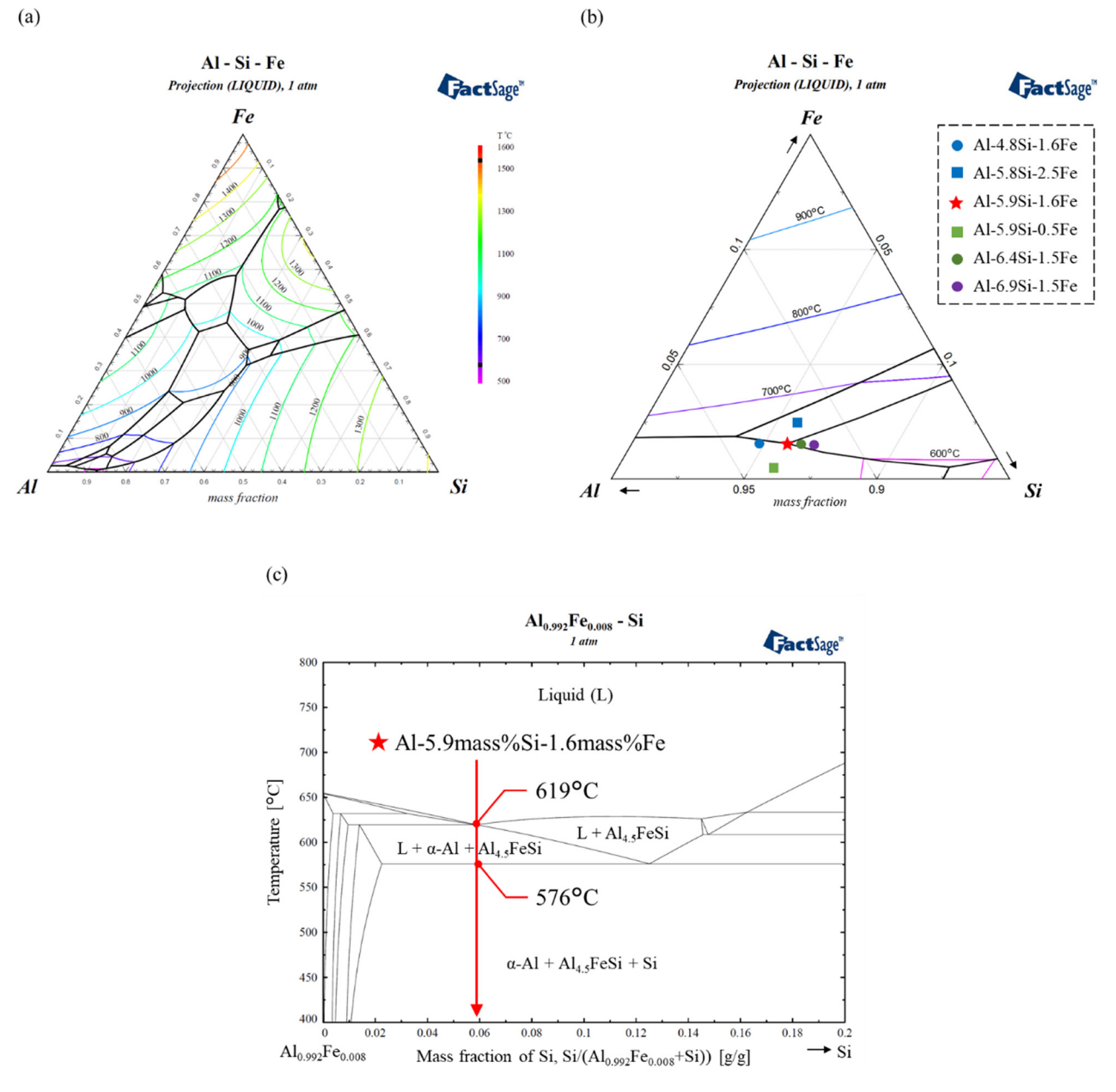


Figure 1: Phase diagram of (a) Al-Si-Fe ternary system, (b) Al-Si-Fe ternary system on Al-rich corner, and (c) Al<sub>0.992</sub>Fe<sub>0.008</sub>-Si on Al<sub>0.992</sub>Fe<sub>0.008</sub>-rich side, which were prepared from the "Phase Diagram" module and the "SGTE 2020 alloy" database in FactSage 8.1 software (the six compositions prepared in this study are illustrated on the (b) Phase diagram of the Al-Si-Fe ternary system on Al-rich corner).

gravitational segregation [21], and controlling the microstructure of Al-Si-Fe intermetallic compounds by adding other elements [21,24] are required.

However, as mentioned previously, Al-containing Fe can be effectively used as a PCM. Naturally, it can also be recycled and used as an LHTES material. Moreover, a process can be proposed to reduce impurity concentration when using Al-based PCM as LHTES material. In that case, it may satisfy the increasing demand for recycling Al alloys in the future. Therefore, the Al-Si-Fe PCM is considered an excellent heat storage material as it is cost-effective and environment-friendly.

Therefore, this study attempted to develop an optimal Al-Si-Fe PCM, a 600°C-class alloy PCM that completely melts below 650°C, with a composition of Al-5.9 mass% Si-1.6 mass% Fe by changing the Si and Fe contents, referring to the phase diagram shown in Figure 1(b) and (c). In addition, we conducted long-term atmospheric exposure tests of the Al-Si-Fe PCM in solid-liquid coexistence and cyclic melting and solidification tests to evaluate the

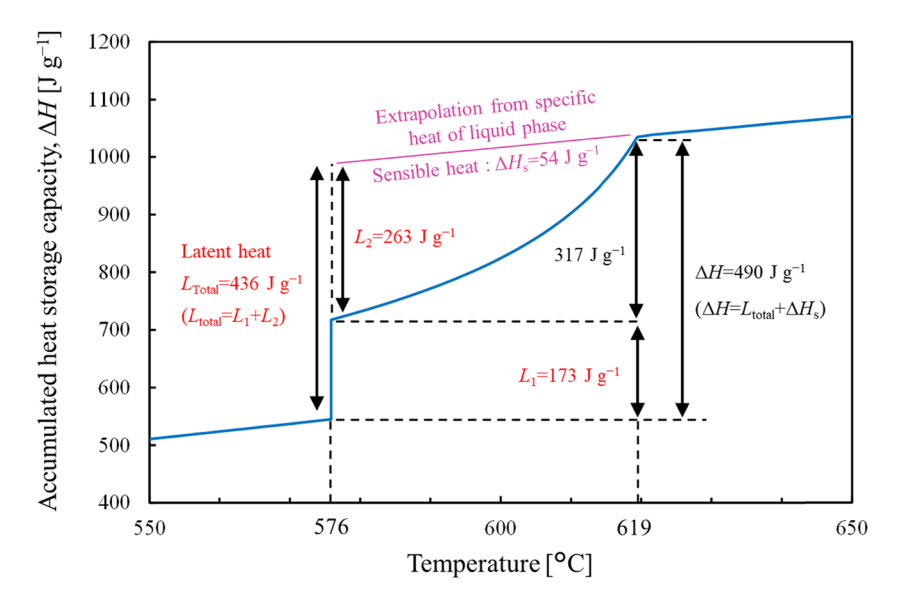


Figure 2: Temperature dependence of the accumulated heat storage capacity (Δ*H*) of Al-5.9 mass% Si-1.6 mass% Fe alloy, which was prepared from the "Equilib" module and the "SGTE 2020 alloy" database in FactSage 8.1 software.

stability of the PCM microstructure and thermal storage performance.

### 2 Materials and methods

#### 2.1 PCM preparation

Granulated Al (99.5%, High Purity Chemistry, Japan), Si (99.999%, High Purity Chemistry, Japan), and Fe (99.98%, Alfa Aesar, United States) were used as raw materials. A total of 10 g was weighed to obtain the six compositions illustrated in Figure 1(b) phase diagram of Al–Si–Fe ternary system on Al-rich corner: Al-4.8Si-1.6Fe, Al-5.9Si-1.6Fe, Al-6.9Si-1.5Fe, Al-5.9Si-0.5Fe, Al-5.8Si-2.5Fe (mass%). The samples were placed in an alumina crucible with a height of 32 mm and an inner diameter of 20 mm. The alloy samples were obtained in an Ar atmosphere at 1,600°C for 5 min in a high-frequency induction furnace. Hereafter, the name of each sample is indicated below by "Composition-PCM." For example, an Al-5.9 mass% Si-1.6 mass% Fe alloy sample is described as Al-5.9Si-1.6Fe-PCM.

#### 2.2 Material characterization

The phase transition temperature, thermal storage, and release properties of the as-prepared PCM were measured using differential scanning calorimetry (DSC) (STA 449 F3

Jupiter, NETZSCH, Germany). For the DSC measurements, samples machined to a diameter of 5.2 mm and a height of 0.1 mm or less were placed in a Pt pan (85  $\mu$ L) with an Al<sub>2</sub>O<sub>3</sub> liner and heated and cooled at  $\pm 5^{\circ}$ C·min<sup>-1</sup> under an Ar flow rate of 50 mL·min<sup>-1</sup>. In that measurement, the sample was heated to 820°C, held for 20 min, and then cooled.

The DSC measurements were taken on samples of all the compositions prepared. However, the other analyses were performed only for Al-5.9Si-1.6Fe-PCM, which was selected as a representative composition.

The sample's density at 25°C ( $\rho_0$ ) was measured using an ultra-pycnometer (Ultrapycnometer 1000, Quantachrome Instruments, United States). The measurement showed that the density ( $\rho_0$ ) of the Al-5.9Si-1.6Fe-PCM sample at 25°C was 2.84 g·cm<sup>-3</sup>. The coefficient of linear thermal expansion ( $\alpha_{\rm CLTE}$ ) of the samples was measured using a thermomechanical analyzer (TMA) (TMA7300, Hitachi High-Tech Science Corporation, Japan). The coefficient of thermal expansion ( $\alpha_{\rm CLTE}$ ) was calculated from the  $\alpha_{\rm CLTE}$  using the following equation:

$$\alpha_{\rm CTE} = 3\alpha_{\rm CLTE}.$$
 (1)

Furthermore, the density ( $\rho$ ) considering the coefficient of thermal expansion was calculated from the following equation:

$$\rho = \rho_0 / (1 + \alpha_{\text{CTE}} (T - T_0)), \tag{2}$$

where T is the sample temperature, and  $T_0$  is 25°C.

Thermal diffusivity ( $\alpha_{TD}$ ) and specific heat ( $C_p$ ) were measured using a laser flash thermal analyzer (TC-7000, ULVAC, Japan). The measurements were taken at 100°C

intervals from 100 to 500°C. The thermal conductivity (k) was calculated from the thermal diffusivity, specific heat, and density using the following equation:

$$k = \alpha_{\rm TD} \times C_{\rm p} \times \rho. \tag{3}$$

The alloy microstructure and elemental distribution were observed using scanning electron microscopy (SEM) and energy-dispersive spectroscopy (EDS) (JSM-7001FA, JEOL Ltd., Japan) on a cross-section of the sample cut through the center of the crucible along the direction of gravity. The observation positions were the bottom and center of the crucible and the top (near the atmosphere's surface). The phase composition was determined via powder X-ray diffraction (XRD) using a 1D silicon strip detector (MiniFlex600, Cu Ka, Rigaku, Japan).

### 2.3 Investigation of phase segregation of PCM in solid-liquid coexistence

Al-5.9Si-1.6Fe-PCM was used as a representative composition, and phase segregation was investigated by maintaining the solid-liquid coexistence for a long time. An electric furnace was used for the tests. The sample was heated to 650°C, held at the same temperature for 1h. It was then cooled to 600°C, maintained for 100 h, and finally cooled to 500°C. The test was conducted in an atmosphere at a heating and cooling rate of 10°C·min<sup>-1</sup>. After cooling to 500°C, the samples were furnace-cooled. The microstructure and elemental distribution of the sample cross-section were observed using SEM and EDS after the test under the same conditions described in Section 2.2.

### 2.4 Investigation of PCM microstructural stability during cyclic melting and solidification

Melting and solidification cycle tests were conducted using an electric furnace (FT-01P, FULL-TECH CO., LTD., Japan) to obtain a representative composition of Al-5.9Si-1.6Fe-PCM. The sample was then heated to 650°C and cooled to 500°C for 100 cycles. The heating and cooling rates were set at 10°C·min<sup>-1</sup>. The test was conducted under three conditions: 1) atmosphere, 2) air (Air, Air Water INC., Japan), and 3) high-purity N<sub>2</sub> (99.9995%, Air Water INC., Japan) in dehydration circulation. For air and N<sub>2</sub> dehydration circulation, the atmosphere was controlled by placing a small electric furnace inside a glove box (UN-800 L; UNICO, Japan).

The air atmosphere was prepared by vacuum displacement of air (Air Water, a high-pressure industrial gas) into a glove box thrice. The melting and solidification cyclic tests were then initiated, and the air was distributed at 250 mL·min<sup>-1</sup> during the test. The humidity was measured using a hygrometer; it was 0.0 and 1.5% relative humidity (RH) at the beginning and end of the test, respectively.

The dehydrated N<sub>2</sub>-circulating atmosphere was prepared by replacing the glove box with high-purity N<sub>2</sub> thrice and then dehydrating the atmosphere for 12 h using a gas circulation purifier (MF-70, UNICO, Japan). Melting and solidification cyclic tests were initiated, and the atmosphere was constantly dehydrated. The humidity during the test was always 0.0% RH.

The microstructure and elemental distribution of the sample cross-section were observed using SEM and EDS after the test under the same conditions described in Section 2.2. In addition, DSC measurements were taken under the same conditions described in Section 2.2 for the samples subjected to cyclic testing under N2 in dehydration circulation.

#### 3 Results

### 3.1 Thermal storage and release performances

Figures 3 and 4 show the DSC curves for (a) heating and (b) cooling of samples with fixed Al-Fe and Al-Si ratios and varying Si and Fe contents, respectively, based on Al-5.9Si-1.6Fe. In addition, Table 1 shows the characteristic values of (a) melting and (b) solidification evaluated from the DSC curves of all compositions of Al-Si-Fe alloy samples. Figures 3(a) and 4(a) show that all the prepared Al-Si-Fe PCM samples have two melting peaks at approximately 580 and 620°C (low-temperature side: P<sub>m1</sub> and hightemperature side:  $P_{m2}$ ). The standard composition sample, Al-5.9Si-1.6Fe-PCM, has latent heat capacities of 204 and 182 J·g $^{-1}$  on the  $P_{\rm m1}$  ( $L_{\rm m1}$ ) and  $P_{\rm m2}$  ( $L_{\rm m2}$ ) sides, respectively, during melting, and the total latent heat capacity ( $L_{m,Total}$ ) is 386 J·g<sup>-1</sup>. On the other hand, from Figures 3(b) and 4(b), three peaks (low-temperature side:  $P_{s1}$ , center:  $P'_{s2}$ , and high-temperature side:  $P_{s2}$ ) are observed between approximately 580 and 620°C during solidification for all Al-Si-Fe PCM samples. The Al-5.9Si-1.6Fe-PCM has latent heat capacities of 158 and 229 J·g<sup>-1</sup> on the  $P_{s1}$  ( $L_{s1}$ ) and the  $P_{s2}$  ( $L_{m2}$ ) sides, respectively, during solidification, and the total latent heat capacity ( $L_{s,Total}$ ) is 387 J·g<sup>-1</sup>. Figures 3(a) and 4(a) show

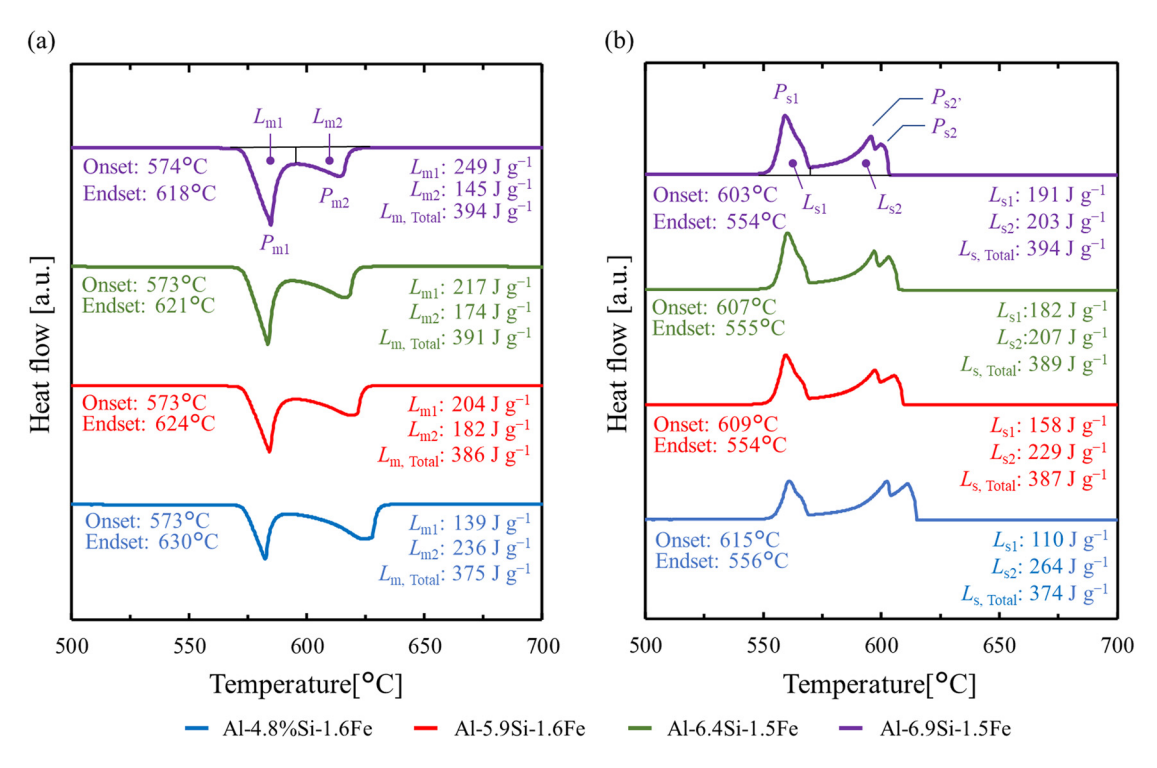


**Figure 3:** DSC curves of (a) heating and (b) cooling of samples with constant Al-Fe ratio and varying Si addition (atmosphere: Ar; flowrate: 50 mL·min<sup>-1</sup>; heating/cooling rate:  $\pm 5 \text{ K·min}^{-1}$ ; sample pan: Al<sub>2</sub>O<sub>3</sub> liner (85  $\mu$ L) in Pt pan (and Pt lid)).

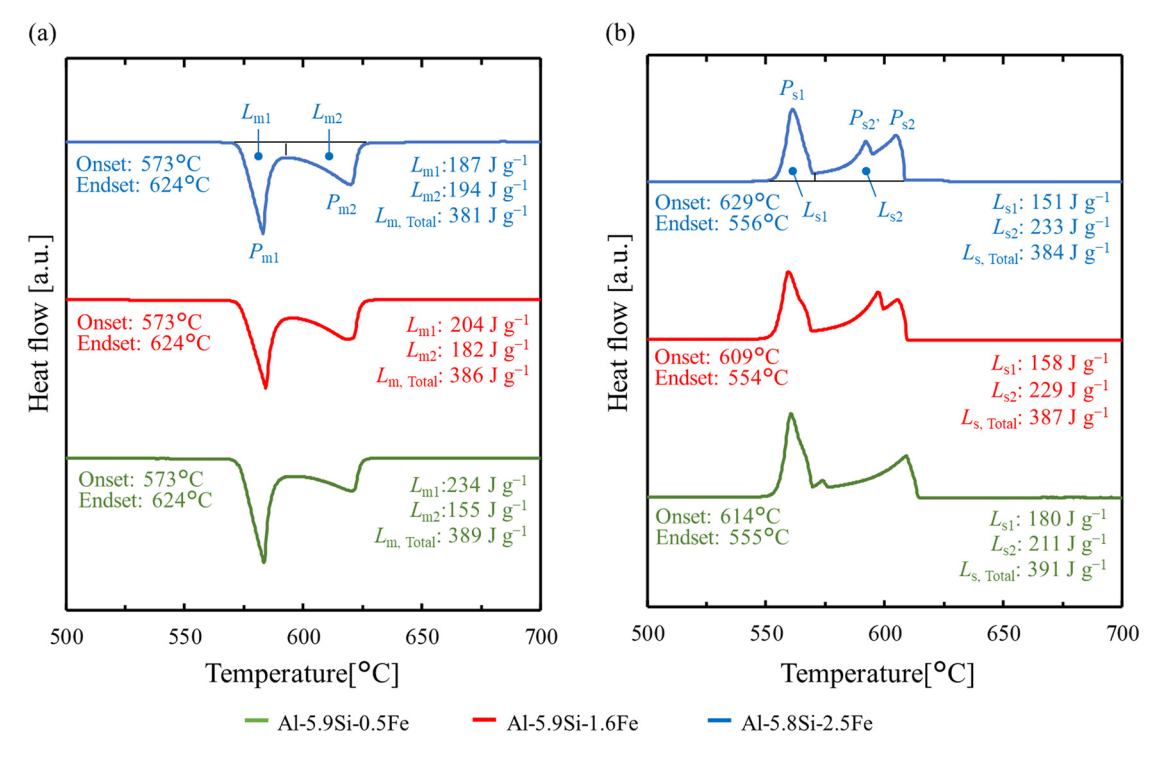


**Figure 4:** DSC curves of (a) heating and (b) cooling of samples with constant Al-Si ratio and varying Fe addition (atmosphere: Ar; flowrate: 50 mL·min<sup>-1</sup>; heating/cooling rate:  $\pm 5 \text{ K·min}^{-1}$ ; sample pan: Al<sub>2</sub>O<sub>3</sub> liner (85  $\mu$ L) in Pt pan (and Pt lid)).

Table 1: Characteristic	values of (a) melting	and (b) solidification for	all the prepared Al-SI-Fe PCM samples	

(a) Melting characteristics							
Composition	Onset [°C]	P <sub>m1</sub> [°C]	P <sub>m2</sub> [°C]	Endset [°C]	L <sub>m1</sub> [J⋅g <sup>-1</sup> ]	L <sub>m2</sub> [J⋅g <sup>-1</sup> ]	L <sub>m, Total</sub> [J·g <sup>-1</sup> ]
Al-4.8Si-1.6Fe	573	582	624	630	139	236	375
Al-5.8Si-2.5Fe	573	583	620	624	187	194	381
Al-5.9Si-1.6Fe	573	584	619	624	204	182	386
Al-5.9Si-0.5Fe	573	584	620	624	234	155	389
Al-6.4Si-1.5Fe	573	584	616	621	217	174	391
Al-6.9Si-1.5Fe	574	585	614	618	249	145	394

#### (b) Solidification characteristics

Composition	Onset [°C]	P <sub>s2</sub> [°C]	P' <sub>s2</sub> [°C]	P <sub>s1</sub> [°C]	Endset [°C]	$L_{\rm s1}$ [J·g <sup>-1</sup> ]	$L_{s2}$ [J·g <sup>-1</sup> ]	L <sub>s, Total</sub> [J∙g <sup>−1</sup> ]
Al-4.8Si-1.6Fe	615	611	602	561	556	110	264	374
Al-5.8Si-2.5Fe	629	605	692	561	556	151	233	384
Al-5.9Si-1.6Fe	609	606	597	560	554	158	229	387
Al-5.9Si-0.5Fe	614	609	574	561	555	180	211	391
Al-6.4Si-1.5Fe	607	603	597	560	555	182	207	389
Al-6.9Si-1.5Fe	603	600	596	559	554	191	203	394

 $P_{s1}$ : low-temperature-side solidification peak;  $P_{s2}$ : high-temperature-side solidification peak;  $P'_{s2}$ : middle solidification peak;  $L_{s1}$ : latent heat of low-temperature-side solidification peak;  $L_{\text{mt}}$ : latent heat of high-temperature-side solidification peak;  $L_{\text{s. Total}}$ : total latent heat of solidification.  $P_{\rm m1}$ : low-temperature-side melting peak;  $P_{\rm m2}$ : high-temperature-side melting peak;.

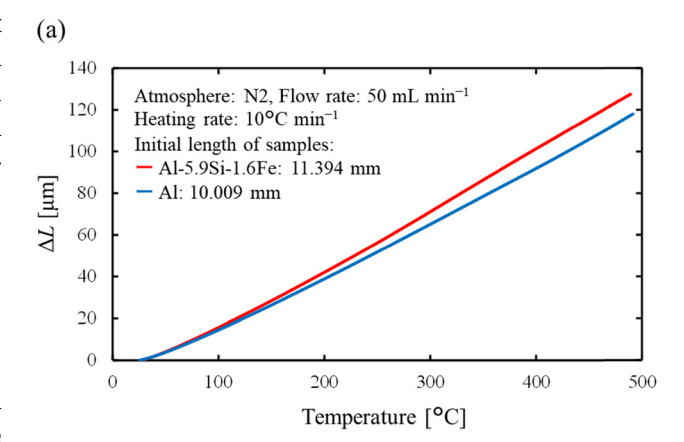
Lmi: Latent heat of low-temperature-side melting peak; Lm2: Latent heat of high-temperature-side melting peak; Lm, Total latent heat of melting.

that the total latent heat is almost equal with varying Si or Fe content. However, the latent heat  $L_{\rm m1}$  and  $L_{\rm s1}$  on the lowtemperature side decreases with increasing Si, whereas  $L_{m1}$ and  $L_{s1}$  increase with increasing Fe content. The endset temperature at the end of melting shifts to the lower temperature side with increasing Si content. As stated earlier, although the ratio of  $L_{\rm m1}$  ( $L_{\rm s1}$ ) to  $L_{\rm m2}$  ( $L_{\rm s2}$ ) is slightly different for different PCM compositions, there is little difference in the total latent heat capacity. Therefore, Al-5.9Si-1.6 Fe found in FactSage 8.1 software was a representative composition in the thermal properties and microstructural stability investigations of 600°C-class Al-Si-Fe PCMs in this study.

### 3.2 Thermal properties

Figure 5 shows the (a) TMA curve and (b) linear expansion coefficient of Al-5.9 Si-1.6 Fe-PCM and Al used as a reference sample. The linear expansion coefficient of the Al-5.9 Si-1.6 Fe-PCM is  $24.6 \times 10^{-6}$ °C in the temperature range of 50 to 480°C, which is approximately 4.3% smaller than that of Al  $(25.7 \times 10^{-6} \, \text{C}^{-1}).$ 

Figure 6 shows the (a) thermal diffusivity and specific heat and (b) thermal conductivity of the Al-5.9Si-1.6Fe-PCM. The thermal diffusivity of Al-5.9Si-1.6Fe-PCM gradually decreases from 0.67 to 0.54 as temperature increases from 100 to 500°C, and the specific heat increases from 0.87 to 1.12 J·g<sup>-1</sup>·K<sup>-1</sup>. The thermal conductivity is approximately 160 W·m<sup>-1</sup>·K<sup>-1</sup> in the same temperature range.



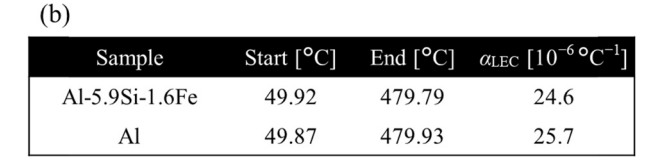
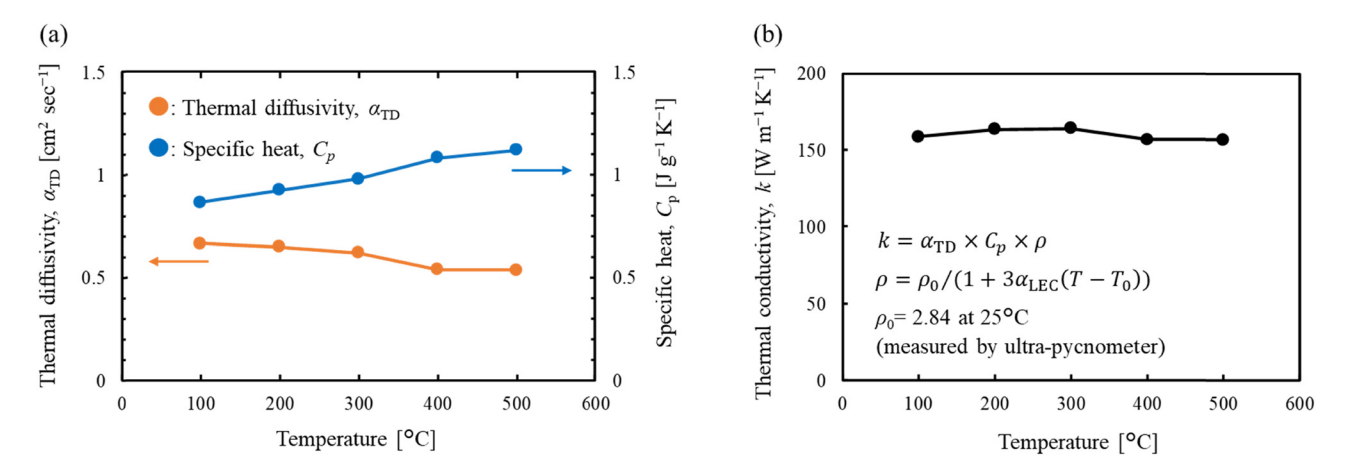


Figure 5: (a) TMA curves and (b) linear expansion coefficient of an Al-5.9Si-1.6Fe-PCM and a reference sample of pure Al.



**Figure 6:** (a) Thermal diffusivity and specific heat and (b) thermal conductivity of Al-5.9Si-1.6Fe-PCM (thermal diffusivity:  $\alpha_{TD}$ ; specific heat:  $C_p$ ; thermal conductivity: k; density: p; density at 25°C:  $p_0$  (2.84 g·cm<sup>-3</sup>); sample temperature: T,  $T_0$ : 25°C).

#### 3.3 Microstructure

Figure 7 shows the SEM images and EDS elemental mapping of (a) mm order and (b)  $\mu$ m order at the top, middle, and bottom of the as-prepared Al-5.9Si-1.6Fe-PCM sample cross-section. From the SEM and EDS observations in Figure 7, the microstructures of the top (Figure 7(a-1, 2),

(b-1, 2)), middle (Figure 7(a-3, 4), (b-3, 4)), and bottom (Figure 7(a-5, 6), (b-5, 6)) of the sample were similar in both the mm and μm orders. EDS mapping of μm order showed that a total of three phases were observed in the top (Figure 7(b-2)), middle (Figure 7(b-4)), and bottom (Figure 7(b-6)) of the sample at any location: an Al-dominant phase, Si crystals and Al–Si–Fe intermetallic

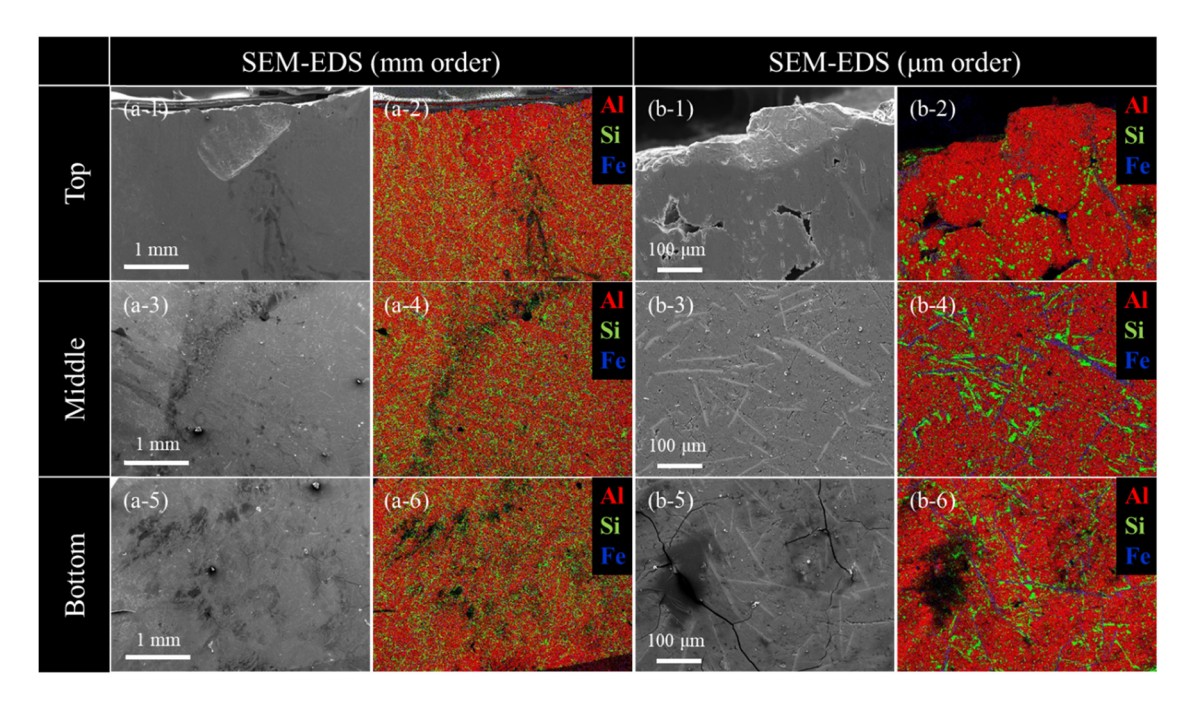


**Figure 7:** SEM images and EDS elemental mapping of (a) mm order and (b) µm order at the top, middle, and bottom of the as-prepared Al-5.9Si-1.6Fe-PCM sample cross-section (in the EDS mapping, red indicates Al, yellow-green indicates Si, and blue indicates Fe).

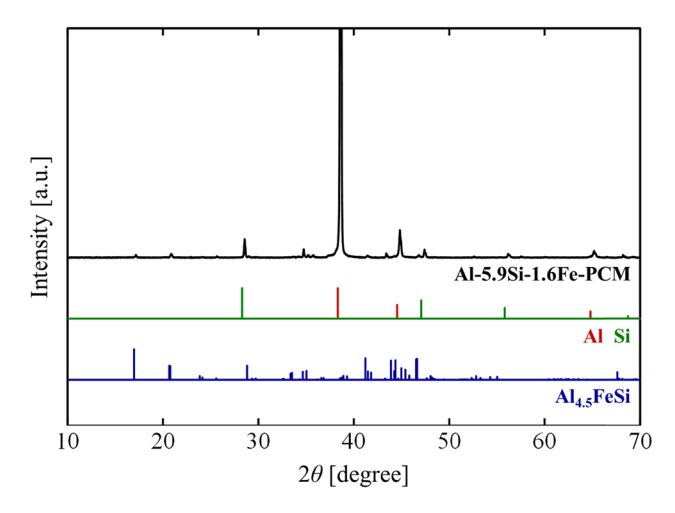
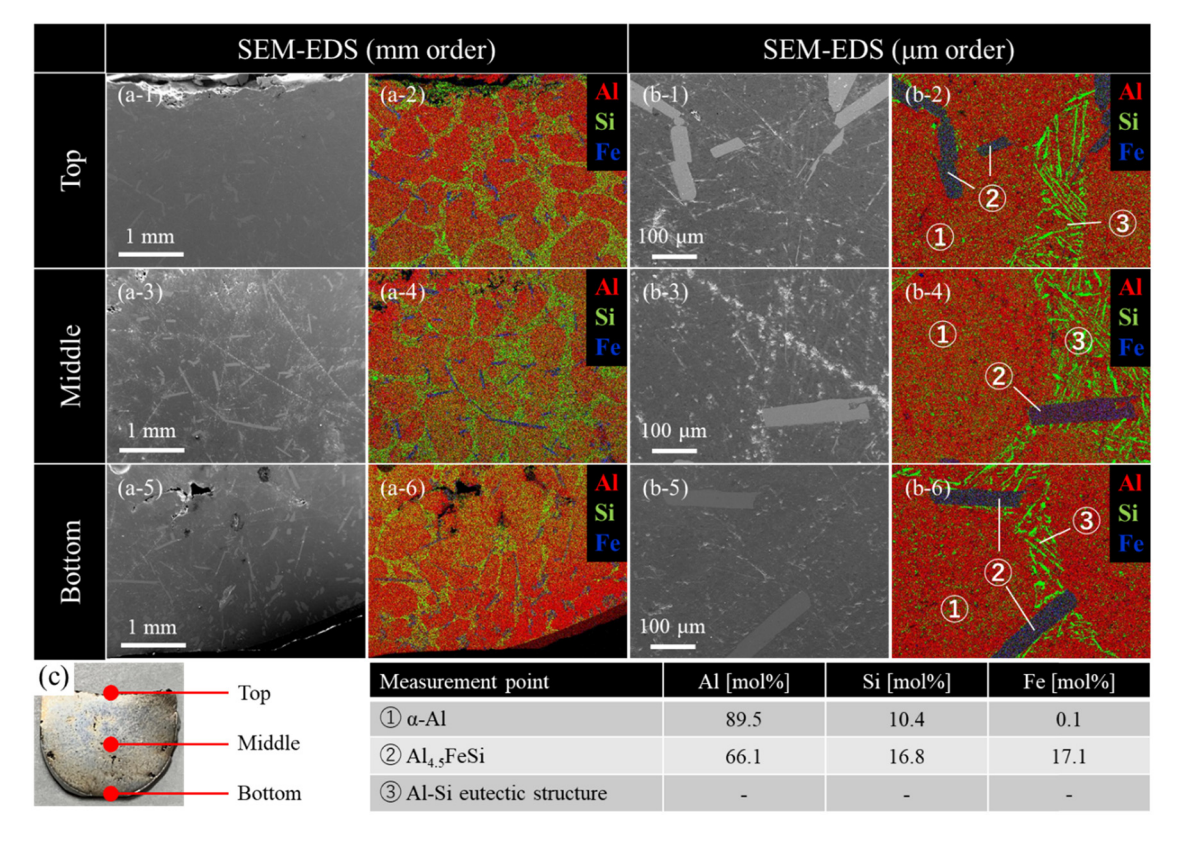


Figure 8: XRD patterns of the Al-5.9Si-1.6Fe-PCM.

compound. Therefore, neither phase was segregated in the sample, and an even microstructure was formed throughout. Figure 8 shows the XRD pattern of the Al-5.9 Si-1.6 Fe-PCM. The XRD patterns detected Al, Si, and Al $_{4.5}$ FeSi phases in the sample.

# 3.4 Microstructure after long-term solid-liquid coexistence

Figure 9 shows the SEM images and EDS elemental mapping of a) mm order and b) μm order at the top, middle, and bottom of the cross-section of Al-5.9Si-1.6Fe-PCM sample after long-time solid-liquid coexistence retention test at 600°C for 100 h in the atmosphere and c) photograph of the sample cross-section. Similar to the microstructure of the as-prepared Al-5.9 Si-1.6 Fe-PCM sample cross-section shown in Figure 7 EDS mapping of the top (Figure 9(a-2), (b-2)), middle (Figure 9(a-4), (b-4)), and lower (Figure 9(a-6), (b-6)) of the sample after long-time solid-liquid coexistence retention test showed a total of three phases: an Al-dominant phase, Si crystals, and Al-Si-Fe intermetallic compound. The three phases, Al and Si and Al-Si-Fe intermetallic compound, were observed evenly at all positions of the top (Figure 9(a-1, 2), (b-1, 2)), middle (Figure 9(a-3, 4), (b-3, 4)), and bottom (Figure 9(a-5, 6), (b-5, 6)) of the sample, and there was no segregation of either phase in the sample, and an even microstructure was formed throughout. However, the microstructure was coarser than the as-prepared



**Figure 9:** SEM images and EDS elemental mapping of (a) mm order and (b) μm order at the top, middle, and bottom of the cross-section of Al-5.9Si-1.6Fe-PCM sample after long-time solid–liquid coexistence retention test at 600°C for 100 h in the atmosphere, and (c) photograph of the sample cross-section (in the EDS mapping, red indicates Al, yellow-green indicates Si, and blue indicates Fe).

Al-5.9Si-1.6Fe PCM sample. The quantitative point analysis results of the Al-dominant phase (1) in Figure 9) and the Al-Si-Fe intermetallic compound phase (2) in Figure 9) are shown in Figure 9. In the ① phase, 89.5% Al, 10.4% Si, and 0.1% Fe were detected, and in the ② phase, 66.1% Al, 16.8% Si, and 17.1% Fe were detected; the phase in the Al-Si-Fe intermetallic compound corresponding to the configuration in ② is Al<sub>4</sub> <sub>5</sub>FeSi [25]. The atomic percentages of Al<sub>4</sub> <sub>5</sub>FeSi are Al-15.4%Fe-15.4%Si, which is generally consistent with the quantitative values for the Al-Fe-Si intermetallic compound shown in Figure 9 (Al-17.1% Fe-16.8% Si). Al<sub>4.5</sub>FeSi is also classified as a phase called  $\tau$  by previous studies, in which the composition of  $\tau$  is indicated by Al<sub>64.5-67.5</sub>Fe<sub>15.5-16.5</sub>Si<sub>17-19</sub> [25]. Considering this point, the difference between the quantitative values of the Al-Fe-Si compounds shown in Figure 9 (Al-17.1% Fe-16.8% Si) and Al-15.4% Fe-15.4% Si can be considered within a small margin of error. Finally, the microstructure in 3 is a eutectic microstructure consisting of the Al phase in ① and two components of Si.

# 3.5 Microstructure after melting and solidification cycles

Figure 10 shows the images of the samples before and after 100 cycles of melt-solidification tests in (a) atmosphere, (b)

air, and (c) dehydrated  $N_2$  circulation. Figure 10(a-1, -2) shows that pores were formed, and the apparent volume expanded inside the sample tested in the atmosphere. Pore formation and apparent volume expansion were also observed in the sample tested in air, although the effect was smaller than in air. Figure 10(c-1, -2) shows that neither void formation nor volume expansion was observed under dehydrated  $N_2$  circulation.

Figure 11 shows the SEM images and EDS elemental mapping of mm and  $\mu m$  orders at the top, middle, and bottom of the cross-section of the Al-5.9Si-1.6Fe-PCM sample after 100 melting and solidification cyclic tests in (a) atmosphere, (b) air, and (c) dehydrated N2 circulation atmosphere. In the SEM observations, porosity was observed in the sample after cyclic testing in the atmosphere and air. However, Al-Si and Al-Si-Fe intermetallic compounds were observed between the top, middle, and bottom without segregation, as well as the microstructure before cyclic testing, as shown in Figure 7. In particular, neither the segregation of specific phases nor porosity was observed in the sample cross-sections that were cyclically tested under dehydrated N<sub>2</sub> circulation. Figure 12 shows the SEM images and EDS quantitative point analysis of a) the dense alloy surface and b) the void-forming area of the Al-5.9Si-1.6Fe-PCM after cyclic testing of melting and solidification in the atmosphere. The surface of the void-forming area had

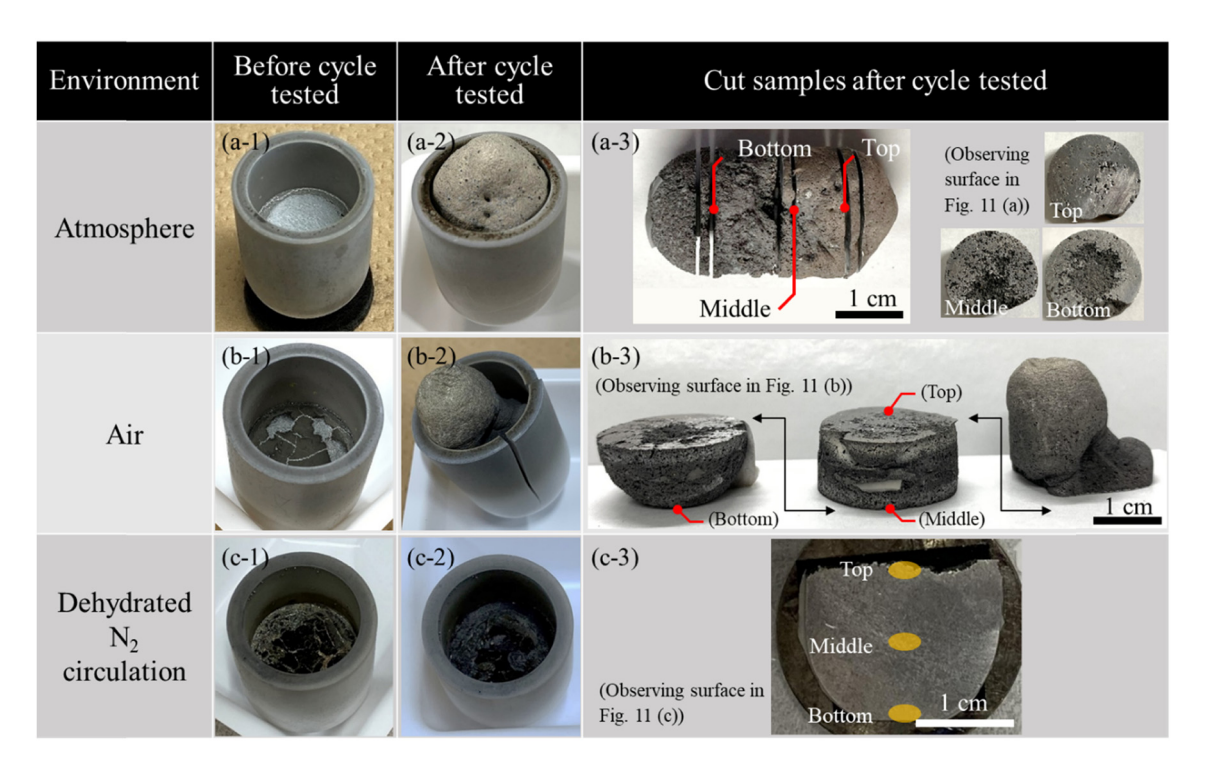


**Figure 10:** Images of samples before and after cyclic testing in (a-1, -2, -3) atmosphere, (b-1, -2, -3) air, and (c-1, -2, -3) dehydrated N<sub>2</sub> circulation, respectively (the top, middle, and bottom points are shown in (a-3), (b-3), and (c-3) correspond to the locations of the SEM-EDS observations in Figure 11).

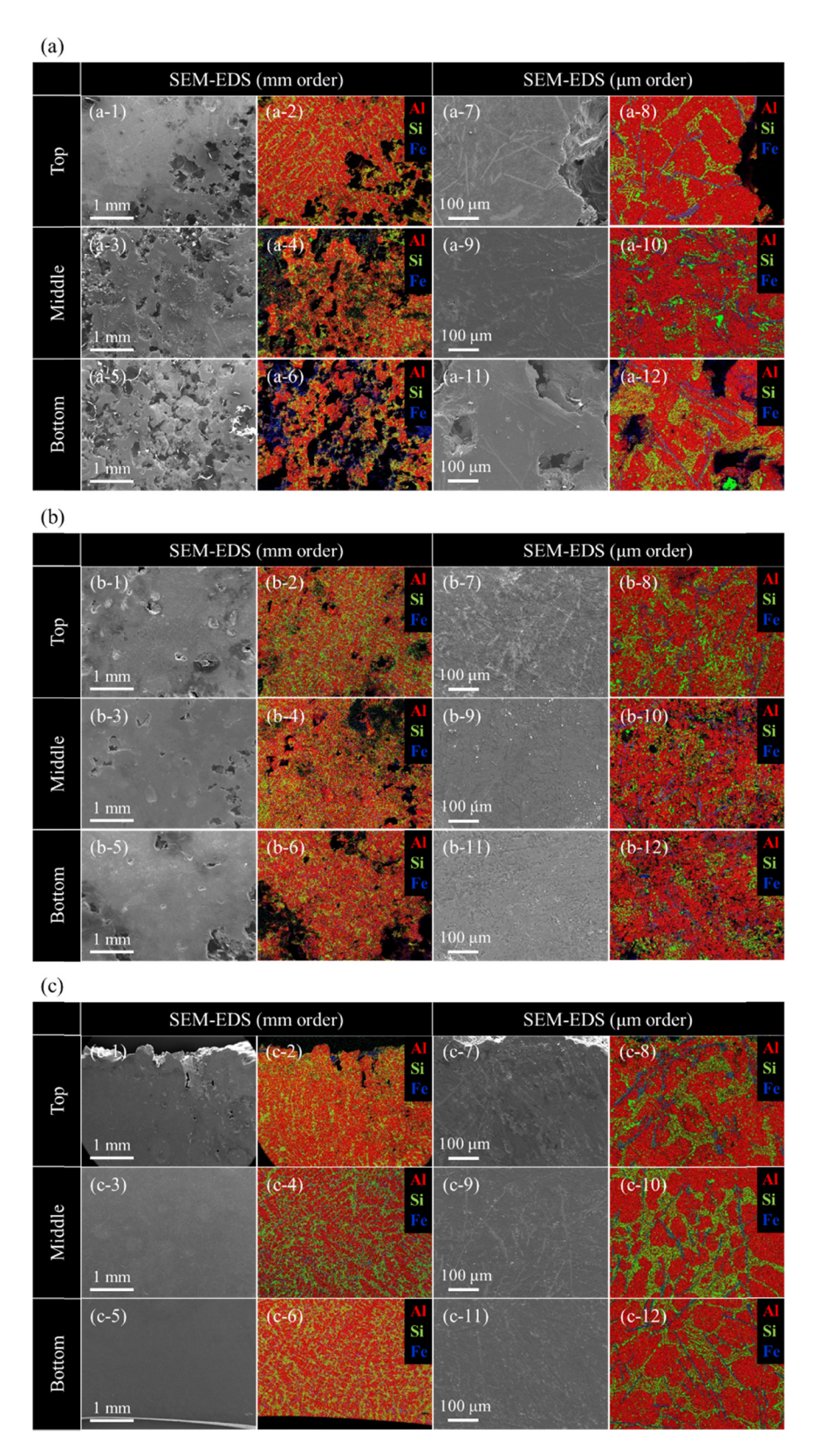
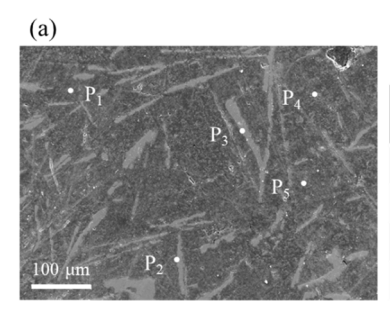
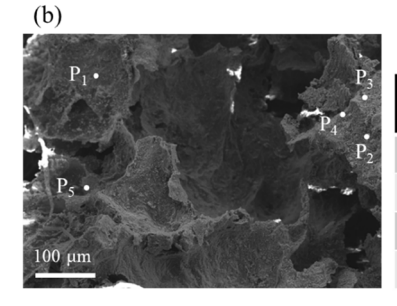


Figure 11: SEM images and EDS elemental mapping of mm and µm orders at the top, middle, and bottom of the cross-section of Al-5.9Si-1.6Fe-PCM sample after 100 melting and solidification cyclic tests in (a) atmosphere, (b) air, and (c) dehydrated N2 circulation atmosphere (the top, middle, and bottom observation points in (a), (b), and (c), respectively, correspond to the sample positions shown in Figure 10(a-3), (b-3), and (c-3)) (in the EDS mapping, red indicates Al, yellow-green indicates Si, and blue indicates Fe).



Composition of alloy surface [mol%]								
Element	$P_1$	P <sub>2</sub>	P <sub>3</sub>	$P_4$	P <sub>5</sub>	Average		
О	9.8	8.6	7.2	10.0	13.4	9.7		
Al	88.2	60.1	62.3	85.4	78.0	74.8		
Si	1.7	14.9	14.5	4.5	7.9	8.7		
Fe	0.3	16.4	16.0	0.2	0.7	6.7		



Composition of the surface forming a void [mol%]								
ement	$\mathbf{P}_1$	P <sub>2</sub>	P <sub>3</sub>	$P_4$	P <sub>5</sub>	Average		
O	17.1	25.3	29.5	34.7	51.0	31.5		
Al	55.1	52.7	46.3	42.5	38.9	47.1		
Si	27.5	21.5	12.0	21.7	5.5	17.6		

12.3

1.0

4.7

3.8

**Figure 12:** SEM images and EDS quantitative point analysis of (a) the alloy dense surface and (b) the void-forming area of Al-5.9Si-1.6Fe-PCM after cyclic testing of melting and solidification in the atmosphere.

0.3

0.6

approximately 22% more O detected in the average composition than the alloy-dense surface.

# 3.6 Cyclic stability of heat storage and release performance

Figure 13 shows the DSC curve after the melting and solidifying cyclic testing of the Al-5.9Si-1.6Fe-PCM sample 100

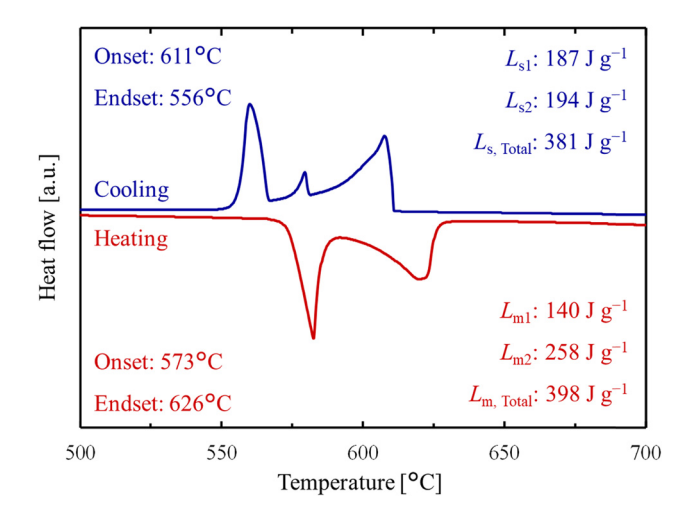


**Figure 13:** DSC curve of the Al-5.9Si-1.6Fe-PCM sample after 100 melting and solidification cyclic tests in a nitrogen atmosphere (atmosphere: Ar; flowrate:  $50 \text{ mL} \cdot \text{min}^{-1}$ ; heating/cooling rate:  $\pm 5 \text{ K} \cdot \text{min}^{-1}$ ; sample pan:  $Al_2O_3$  liner (85  $\mu$ L) in Pt pan (and Pt lid).

times in dehydrated  $N_2$  circulation. The Al-5.9Si-1.6Fe-PCM sample after 100 cycle tests melted in two steps from 573 to 626°C and solidified in three steps from 611 to 556°C, similar to the sample before the cyclic test, as shown in Figures 2 and 3. Thus, there was no degradation in the heat storage performance of the Al-5.9Si-1.6Fe-PCM, even after repeated melting and solidification. However, comparing the latent heat capacities separated into low-temperature ( $L_{\rm m1}$ ,  $L_{\rm s1}$ ) and high-temperature ( $L_{\rm m2}$ ,  $L_{\rm s2}$ ) sides, the ratio of the high-temperature-side latent heat capacities ( $L_{\rm m2}$  and  $L_{\rm s2}$ ) to the total latent heat capacities ( $L_{\rm m3}$ ,  $L_{\rm t01}$ ) increased for the Al-5.9Si-1.6Fe-PCM after 100 cycles of testing.

#### 4 Discussion

## 4.1 Microstructure formation process during solidification

The DSC curve of the Al–Si–Fe alloy PCM shown in Figure 3 shows two melting peaks ( $P_{\rm m1}$  and  $P_{\rm m2}$ ), whereas three peaks ( $P_{\rm s2}$ ,  $P_{\rm s2}$ , and  $P_{\rm s1}$ ) were observed for solidification. The melting reaction is explained by the eutectic reaction at 576°C ( $P_{\rm m1}$ ) and the subsequent melting reaction of Al and Al<sub>4.5</sub>FeSi up to 619°C ( $P_{\rm m2}$ ), as shown in Figure 1(b). In contrast, the solidification reaction eventually yielded equilibrium phases of Al, Si, and Al<sub>4.5</sub>FeSi, but unlike

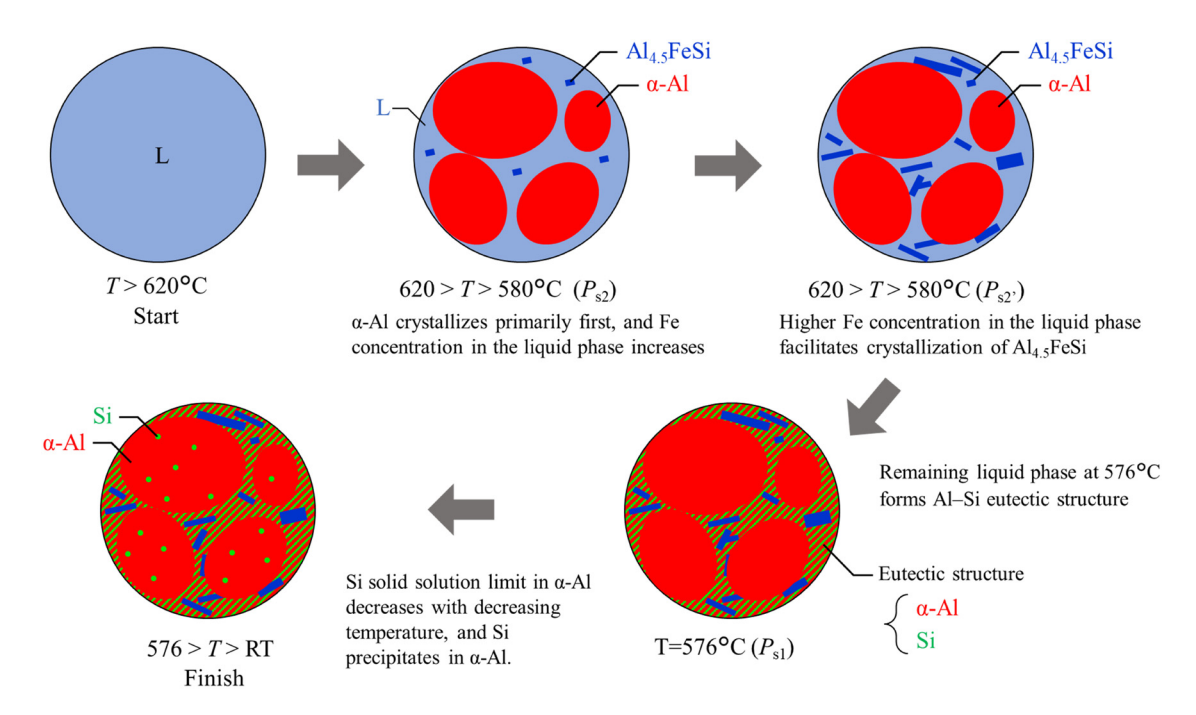


Figure 14: Schematic diagram of the microstructure formation process during solidification of Al-Si-Fe alloy PCM.

melting, it occurred in three stages. Therefore, we discuss a three-step solidification mechanism. Figure 14 shows a schematic of the solidification process of the Al-Si-Fe alloy PCM. When the Al-Si-Fe PCM is cooled from the liquid state to below 620°C, an Al solid solution (α-Al) crystallizes. A certain amount of Si dissolves in α-Al, but almost no Fe is soluble in  $\alpha$ -Al. Consequently, the Fe concentration in the liquid phase increases as  $\alpha$ -Al crystallizes, facilitating the crystallization of Al<sub>4.5</sub>FeSi. According to the equilibrium theory, α-Al and Al<sub>4.5</sub>FeSi should crystallize simultaneously. However, because the Fe content in the alloy is much lower than that of Al. it can be inferred that the coagulation for crystallization would be delayed compared to that of Al. As the temperature decreases to 576°C, the liquid phase forms a eutectic structure of α-Al and Si. In the phase diagram, the eutectic structure consists of three phases, including Al<sub>4.5</sub>FeSi; however, in the case of Al-5.9Si-1.6Fe, the amount is considerably small. After the Al-Si-Fe alloy PCM is completely solidified, Si precipitation may occur owing to the decrease in the Si solid solution limit of  $\alpha$ -Al with cooling. Therefore, the three solidification peaks in the DSC curves of the cooling of the Al-Si-Fe PCM in Figures (2-b) and (3-b) were determined to be due to the crystallization of  $\alpha$ -Al in  $P_{s2}$ , Al<sub>4.5</sub>FeSi in  $P_{s2}$ , and the eutectic reaction of  $\alpha$ -Al and Si in  $P_{s1}$ , respectively.

### 4.2 Microstructural stability in solid-liquid coexistence

As described in Section 3.4, the Al-5.9Si-1.6Fe-PCM was characterized by equilibrium phases even after being treated at 600°C for 100 h in solid-liquid coexistence. There was no phase segregation because segregation of a particular phase was observed. However, previous studies have shown that Al<sub>4.5</sub>FeSi may precipitate and segregate in Al–Si–Fe alloys depending on their composition [21,23]. In an earlier study using an Al-10% Si-2% Fe alloy, segregation of Al<sub>4.5</sub>FeSi was observed even after maintaining the alloy at 600°C for only 2h in a solid-liquid coexisting state [21]. However, such phase separation should be accompanied by gravitational segregation of Al<sub>4.5</sub>FeSi and the liquid phase in a two-phase state in the alloy system or filtration of Al<sub>4.5</sub>FeSi that crystallized as the primary crystal [21,23]. In this study, Al<sub>4.5</sub>FeSi did not phase-segregate because α-Al was also present in the liquid at the same time when Al<sub>4.5</sub>FeSi crystallized, as shown in the phase diagram in Figure 1(b). Furthermore, if the solidification mechanism shown in Figure 14 is correct, the solidification process of Al-5.9 Si-1.6Fe-PCM, Al<sub>4.5</sub>FeSi crystallizes after α-Al crystallizes as the primary crystal. Thus, phase separation due to gravitational segregation of Al<sub>4.5</sub>FeSi is unlikely to occur. Therefore, the Al-5.9Si-1.6Fe-PCM can be used as a stable LHTES material because

the segregation of certain phases does not occur even if the solid–liquid coexistence state between approximately 580 and 620°C is maintained for a long time.

# 4.3 Microstructural changes and stability during melt-solidification cycle tests

As described in Section 3.5, porosities were observed in the sample after 100 cycles of melting and solidification tests of Al-5.9Si-1.6Fe-PCM in the atmosphere or air. Moreover, the porous alloy surface was oxidized. There are two possible causes for the formation of porosity in the sample – the effect of the volume change of material expansion and shrinkage associated with solid—liquid phase transformation and the bubbling of hydrogen dissolved in the alloy.

First, the porosity formation due to volume expansion and shrinkage associated with the solid—liquid phase transformation is attributed to the formation of oxides on the alloy surface during the cyclic tests, inhibiting the shape change of the sample. The alloy sample undergoes volumetric expansion during the liquid-phase transformation associated with temperature rise. In contrast, the oxide formed during the volumetric expansion may inhibit the movement of the liquid surface and the interface between the surface and crucible during shrinkage associated with solidification. Therefore, the volume shrinkage because of solidification could be compensated for by the formation of pores inside the sample, resulting in an apparent volume expansion.

The formation of porosity due to hydrogen bubbling is caused by the hydrogen produced by the reaction between Al and atmospheric water vapor, as shown in the following equation [26]:

$$2Al + 3H_2O \rightarrow Al_2O_3 + 6H.$$
 (4)

The hydrogen produced by the reaction in the aforementioned equation dissolves into the molten Al alloy; the Al alloy forms porosities by trapping its solid-solution hydrogen during solidification. In particular, Al alloys are difficult to desorb even though hydrogen is easily soluble in Al alloys because the gap between the liquid solids in the solid hydrogen solution at the melting point is large, and the alumina film inhibits hydrogen permeation [27].

Therefore, in conventional Al-alloy castings and forgings, porosities caused by hydrogen trapping are identified as a problem that reduces the quality of the product. In this study, the amount of porosity formation in the Al-5.9Si-1.6Fe-PCM was lower in the air than in the atmosphere. Furthermore, no porosity was observed in the samples

repeatedly tested under dehydrated N2 circulation. Therefore, the solid solution of hydrogen and bubbling of hydrogen significantly influence the porosity formation. We inferred that the effect of porosity formation was particularly pronounced in this study because the melting and solidification processes were repeated 100 times, which is not usually followed in the manufacturing process of Al alloy products. Thus, the melting and solidification cyclic tests in the atmosphere or air led to problems of porosity formation and volume expansion in the Al-Si-Fe alloy PCM. In contrast, the cyclic tests under dehydrated N<sub>2</sub> circulation caused neither the problem nor any segregation of specific phases. Therefore, it can be inferred that the Al-Si-Fe PCM can be considered microstructurally stable and repeatedly used by avoiding the porosity formation caused by inhibiting shape changes due to oxides on the alloy surface and hydrogen trapping.

Furthermore, as described in Section 3.6, the total latent heat of the Al-5.9Si-1.6Fe-PCM did not decrease after repeated testing; however, the high-temperature-side latent heat ( $L_{\rm m2}$  and  $L_{\rm s2}$ ) in the total latent heat increased. This is attributed to the compositional irregularities in the alloy sample; however, as mentioned earlier, no microstructural segregation was observed. Moreover, the melting and solidification of the sample after cyclic testing occur in two or three steps from approximately 580 to 620°C, which is the same not only for the Al-5.9Si-1.6Fe-PCM but also for all the Al–Si–Fe PCM samples prepared with different compositions. In other words, slight changes in the phase-change behavior owing to melt–solidification cyclic tests do not pose a problem when using Al–Si–Fe alloys as 600°C-class PCMs.

The abovementioned microstructural stabilities, such as void formation and segregation in Al-Si-Fe PCM, were discussed. It was shown that the apparent volume expansion of the PCM during repeated melting and solidification could be overcome by avoiding oxidation and hydrogen dissolution by using the PCM in an inert atmosphere. If the Al-Si-Fe PCM could be made available in non-inert atmospheres, it would be easier to use as a 600°C-class LHTES material. Encapsulation of Al-Si-Fe PCM is one promising option for that technique. Encapsulated alloybased PCMs for high-temperature LHTES have been reported in various sizes ranging from µm to cm order using such alloys as Zn-based [28], Al-based (e.g., Al [29,30], Al-Si [31,32], Al-Ni [33] and Al-Zn [34]) and Cu-based (e.g., Cu [35] and Cu-Al [36]) alloys. Encapsulation of alloy-based PCM is expected to prevent the oxidation and hydrogen dissolution of PCM, which were problems in this study, even in a non-inert atmosphere. Furthermore, the problems of phase separation due to the segregation of certain phases in PCMs, which concerns macro-scale PCMs, may not be a problem when PCMs are encapsulated. This is because encapsulated PCMs undergo phase change only inside each capsule, and phase separation does not occur on a scale more significant than the capsule size. Therefore, there is a concern that macro-scale PCM may cause largescale phase separation and uneven thermal properties depending on the size. However, for small encapsulated PCM in the range of µm to cm order, phase separation is impossible beyond the size of each capsule. Thus, there is no need to be concerned about phase separation. In particular, microencapsulation using self-oxidation has been reported for Al alloys in a variety of compositions, such as Al [29,30], Al-Si [31], Al-Ni [33], and Al-Zn [28,34]. From the aforementioned facts, microencapsulation of alloys is an especially promising option to use Al-Si-Fe PCMs in a microstructurally stable manner, not limited to inert atmospheres.

**DE GRUYTER** 

# 4.4 Comparison with conventional heat storage material

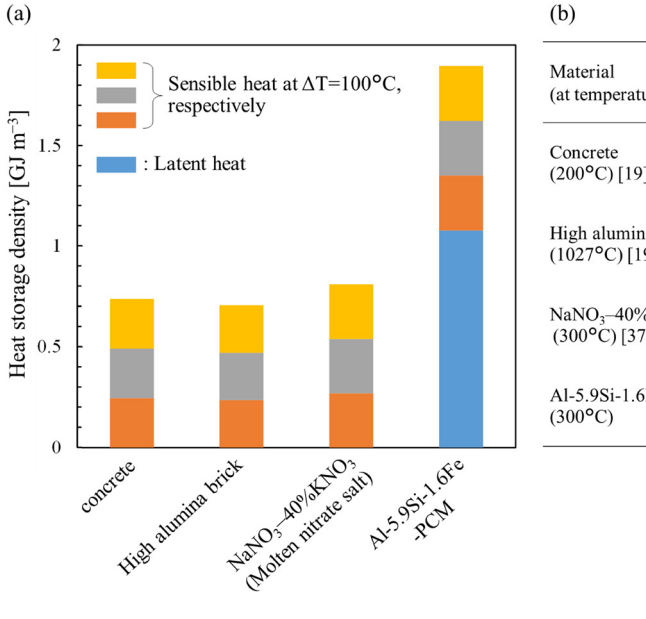
Figure 15 shows a) a comparison of the volume-based heat storage densities of the conventional SHTES materials of concrete, high alumina brick, and solar salt, and Al-5.9Si-1.6Fe-PCM in this study at  $\Delta T = 300^{\circ}$ C and b) their respective physical properties. The Al-5.9Si-1.6Fe-PCM has more

than twice the heat storage density of conventional SHTES materials, even when assuming a  $\Delta T$  of 300°C. Therefore, the Al-Si-Fe PCM can be used to design a more compact heat storage system with a higher heat storage density than that of conventional SHTES materials. Generally, a smaller heat storage system is expected to reduce the heat exchange rate because of the smaller heat transfer area for heat exchange; however, this is not a problem in the case of the Al-Si-Fe PCM. This is because the thermal conductivity of Al-5.9Si-1.6Fe-PCM (164 W·m<sup>-1</sup>·K<sup>-1</sup>) is much higher than that of conventional SHTES materials such as alumina brick  $(9.7 \text{ W}\cdot\text{m}^{-1}\cdot\text{K}^{-1} \text{ [19]})$  and solar salt  $(\text{NaNO}_2-40\%\text{KNO}_3)$  $(0.6 \text{ W}\cdot\text{m}^{-1}\cdot\text{K}^{-1} [37])$ , as shown in Figure 15(b). Therefore, the Al-Si-Fe PCM can be designed to have a more compact and rapid heat exchange TES system than conventional SHTES materials.

#### 5 Conclusion

In this study, we investigated an Al–Si–Fe PCM that melts until 620°C; this is suitable for a Carnot battery that reuses the ultra-supercritical steam turbine of coal-fired power generation. The main conclusions are as follows.

 There was no significant difference in the heat storage performance, including the total latent heat capacity, among the six compositions of Al-Si-Fe PCMs in this study. Therefore, Al-5.9Si-1.6Fe found in FactSage 8.1



Material (at temperature) [Ref.]	Density [kg m <sup>-3</sup> ]	Specific heat $[J g^{-1} K^{-1}]$	Thermal conductivity [W m <sup>-1</sup> K <sup>-1</sup> ]
Concrete (200°C) [19]	2700	0.91	1.0
High alumina brick (1027°C) [19]	2200	1.07	9.7
NaNO <sub>3</sub> –40%KNO <sub>3</sub> (Liquid) (300°C) [37]	1730	1.54	0.6
Al-5.9Si-1.6Fe-PCM (300°C)	2790	0.98	164

**Figure 15:** (a) Heat storage density per volume at  $\Delta T = 300^{\circ}$ C for conventional solid and liquid sensible heat storage materials and Al-5.9Si-1.6Fe-PCM and (b) physical properties of various heat storage materials.

software was used as a representative composition in the investigations of thermal properties and microstructural stability of 600°C-class Al–Si–Fe PCMs.

- The Al-5.9Si-1.6Fe-PCM melted in two steps from 573 to 624°C and had a high latent heat capacity of 386 J·g<sup>-1</sup>. The thermal conductivity in the high-temperature solid state was approximately 160 W·m<sup>-1</sup>·K<sup>-1</sup>, which is tens to hundreds of times higher than that of conventional solid or liquid SHTES materials such as alumina bricks and molten nitrate salts.
- The Al-5.9Si-1.6Fe-PCM showed no segregation in the PCM after a high-temperature holding test at 600°C for 100 h in solid–liquid coexistence and 100 cycles of melting and solidification tests in dehydrated N<sub>2</sub> circulation. In addition, the Al-5.9Si-1.6Fe-PCM maintained its original latent heat storage capacity after repeated melting and solidification tests in dehydrated N<sub>2</sub> circulation.
- The repeated melting and solidification of Al-5.9Si-1.6Fe-PCM under atmospheric conditions caused the accompanying volume expansion and shrinkage and oxidation of the alloy by oxygen and water vapor and solid solution and bubbling of hydrogen. This resulted in porosity formation inside the PCM. Porosity formation was eliminated under dehydrated N<sub>2</sub> circulation. In other words, porosity formation and volume expansion are not problematic when the PCM is used in an inert or closed system rather than in an open atmosphere.
- The Al-5.9Si-1.6Fe-PCM has a heat storage density on a volume basis that is more than twice that of conventional SHTES materials such as alumina bricks and molten nitrate salt, even when a  $\Delta T$  of 300°C is assumed.

Thus, the Al–Si–Fe PCM can be applied to high-temperature heat applications such as the Carnot battery. In the future, the encapsulation of the Al–Si–Fe PCM and the development of corrosion suppression technology by slurry introduction are expected to make the Al–Si–Fe PCM an even more versatile LHTES material.

**Acknowledgements:** A part of this work was conducted at Hokkaido University, supported by the "Nanotechnology Platform" Program of the Ministry of Education, Culture, Sports, Science and Technology (MEXT), Japan.

**Funding information:** This article is based on results from a project (No. JPNP16002) subsidized by the New Energy and Industrial Technology Development Organization (NEDO).

**Author contributions:** Yuto Shimizu: writing – original draft, writing – review and editing, investigation, data

curation; Takahiro Nomura: writing – review and editing, supervision, project administration, methodology, investigation, funding acquisition, formal analysis, conceptualization.

**Conflict of interest:** The authors state no conflict of interest.

**Data availability statement:** The datasets generated during and/or analyzed during this study are available from the corresponding author upon request.

#### References

- [1] Ren, G., J. Liu, J. Wan, Y. Guo, and D. Yu. Overview of wind power intermittency: Impacts, measurements, and mitigation solutions. *Applied Energy*, Vol. 204, 2017, pp. 47–65.
- [2] Argyrou, M. C., P. Christodoulides, and S. A. Kalogirou. Energy storage for electricity generation and related processes: Technologies appraisal and grid scale applications. *Renewable and Sustainable Energy Reviews*, Vol. 94, 2018, pp. 804–821.
- [3] Steinmann, W.-D. Thermo-mechanical concepts for bulk energy storage. Renewable and Sustainable Energy Reviews, Vol. 75, 2017, pp. 205–219.
- [4] Steinmann, W.-D., H. Jockenhöfer, and D. Bauer. Thermodynamic analysis of high-temperature carnot battery concepts. *Energy Technology*, Vol. 8, 2020, id. 1900895.
- [5] Dumont, O., G. F. Frate, A. Pillai, S. Lecompte, M. De Paepe, and V. Lemort. Carnot battery technology: A state-of-the-art review. *Journal of Energy Storage*, Vol. 32, 2020, id. 101756.
- [6] Electric Thermal Energy Storage (ETES) ETES:SWITCH, (n.d.). https:// www.siemensgamesa.com/products-and-services/hybrid-andstorage/thermal-energy-storage-with-etes-switch (accessed lanuary 26, 2022).
- [7] Novotny, V., V. Basta, P. Smola, and J. Spale. Review of carnot battery technology commercial development. *Energies*, Vol. 15, No. 2, 2022, id. 647. Multidisciplinary Digital Publishing Institute.
- [8] Technology SaltX Technology World patented nano-technology, SaltX Technology. (n.d.). https://saltxtechnology.com/technology/ (accessed February 24, 2022).
- [9] RWE, Liquid salt storage facilities, (n.d.). https://www.rwe.com/en/ press/rwe-power/2019-03-15-liquid-salt-storage-facilities-(accessed February 24, 2022).
- [10] Cao, R., Y. Lu, D. Yu, Y. Guo, W. Bao, Z. Zhang, et al. A novel approach to improving load flexibility of coal-fired power plant by integrating high temperature thermal energy storage through additional thermodynamic cycle. *Applied Thermal Engineering*, Vol. 173, 2020, id. 115225.
- [11] Fan, H., Z. Zhang, J. Dong, and W. Xu. China's R&D of advanced ultra-supercritical coal-fired power generation for addressing climate change. *Thermal Science and Engineering Progress*, Vol. 5, 2018, pp. 364–371.
- [12] Rogalev, N., A. Golodnitskiy, A. Tumanovskiy, and A. Rogalev. A survey of state-of-the-art development of coal-fired steam turbine power plant based on advanced ultrasupercritical steam technology. *Contemporary Engineering Sciences*, Vol. 34, 2014, pp. 1807–1825.

- [13] Alva, G., L. Liu, X. Huang, and G. Fang. Thermal energy storage materials and systems for solar energy applications. Renewable and Sustainable Energy Reviews, Vol. 68, 2017, pp. 693-706.
- [14] Guillot, S., A. Faik, A. Rakhmatullin, J. Lambert, E. Veron, P. Echegut, et al. Corrosion effects between molten salts and thermal storage material for concentrated solar power plants. Applied Energy, Vol. 94, 2012, pp. 174-181.
- [15] Prieto, C., R. Osuna, A. I. Fernández, and L. F. Cabeza. Thermal storage in a MW scale. Molten salt solar thermal pilot facility: Plant description and commissioning experiences. Renewable Energy, Vol. 99, 2016, pp. 852-866.
- [16] Mohamed, S. A., F. A. Al-Sulaiman, N. I. Ibrahim, Md. H. Zahir, A. Al-Ahmed, R. Saidur, et al. A review on current status and challenges of inorganic phase change materials for thermal energy storage systems. Renewable and Sustainable Energy Reviews, Vol. 70, 2017, pp. 1072-1089.
- [17] Costa, S. C. and M. Kenisarin. A review of metallic materials for latent heat thermal energy storage: Thermophysical properties, applications, and challenges. Renewable and Sustainable Energy Reviews, Vol. 154, 2022, id. 111812.
- [18] Wei, G., G. Wang, C. Xu, X. Ju, L. Xing, X. Du, et al. Selection principles and thermophysical properties of high temperature phase change materials for thermal energy storage: A review. Renewable and Sustainable Energy Reviews, Vol. 81, 2018, pp. 1771-1786.
- [19] Japan Society of Thermophysical Properties. Thermophysical properties handbook, Yokendo Co. Ltd., 2008.
- [20] Raabe, D., D. Ponge, P. J. Uggowitzer, M. Roscher, M. Paolantonio, C. Liu, et al. Making sustainable aluminum by recycling scrap: The science of "dirty" alloys. Progress in Materials Science, Vol. 128, 2022, id. 100947.
- [21] Basak, C. B. and N. Hari Babu. Morphological changes and segregation of β-Al9Fe2Si2 phase: A perspective from better recyclability of cast Al-Si alloys. Materials & Design, Vol. 108, 2016, pp. 277-288.
- [22] Gaustad, G., E. Olivetti, and R. Kirchain. Improving aluminum recycling: A survey of sorting and impurity removal technologies. Resources, Conservation and Recycling, Vol. 58, 2012, pp. 79–87.
- [23] de Moraes, H. L., J. R. de Oliveira, D. C. R. Espinosa, and J. A. S. Tenório. Removal of iron from molten recycled aluminum through intermediate phase filtration. Materials Transactions, Vol. 47, 2006, pp. 1731-1736.
- [24] Shabestari, S. G. The effect of iron and manganese on the formation of intermetallic compounds in aluminum-silicon alloys. Materials Science and Engineering: A, Vol. 383, 2004, pp. 289–298.
- [25] Krendelsberger, N., F. Weitzer, and J. C. Schuster. On the reaction scheme and liquidus surface in the ternary system Al-Fe-Si. *Metallurgical and Materials Transactions A*, Vol. 38, 2007, pp. 1681–1691.

- [26] Harvey, J.-P. and P. Chartrand. Modeling the hydrogen solubility in liquid aluminum alloys. Metall Mater Trans B, Vol. 41, 2010, pp. 908-924.
- [27] Talbot, D. E. J. Effects of hydrogen in aluminium, magnesium, copper, and their alloys. International Metallurgical Reviews, Vol. 20, 1975, pp. 166-184. Taylor & Francis.
- [28] Kawaguchi, T., H. Sakai, R. Ishida, Y. Shimizu, A. Kurniawan, and T. Nomura. Development of core-shell type microencapsulated phase change material with Zn-30 mass% Al alloy and its shell formation mechanism. Journal of Energy Storage, Vol. 55, 2022, id. 105577.
- [29] Nomura, T., J. Yoolerd, N. Sheng, H. Sakai, Y. Hasegawa, M. Haga, et al. Al/A<sub>12</sub>O<sub>3</sub> core/shell microencapsulated phase change material for high-temperature applications. Solar Energy Materials and Solar Cells, Vol. 193, 2019, pp. 281-286.
- [30] Li, Q., X. Ma, X. Zhang, J. Ma, J. Liu, X. Hu, et al. Preparation and properties of  $AI/AI_2O_3$  core-shell microencapsulated phase change material. Journal of Alloys and Compounds, Vol. 888, 2021, id. 161606.
- [31] Nomura, T., C. Zhu, N. Sheng, G. Saito, and T. Akiyama. Microencapsulation of metal-based phase change material for high-temperature thermal energy storage. Sci Rep, Vol. 5, No. 1, 2015, id. 9117. Nature Publishing Group.
- Fukahori, R., T. Nomura, C. Zhu, N. Sheng, N. Okinaka, and [32] T. Akiyama. Macro-encapsulation of metallic phase change material using cylindrical-type ceramic containers for high-temperature thermal energy storage. Applied Energy, Vol. 170, 2016, pp. 324-328.
- Shimizu, Y., T. Kawaguchi, H. Sakai, K. Dong, A. Kurniawan, and T. Nomura. Al-Ni alloy-based core-shell type microencapsulated phase change material for high temperature thermal energy utilization. Solar Energy Materials and Solar Cells, Vol. 246, 2022,
- [34] Li, Q., X. Ma, X. Zhang, J. Ma, X. Hu, and Y. Lan. Microencapsulation of Al-Zn alloy as phase change materials for high-temperature thermal storage application. Materials Letters, Vol. 308, 2022,
- [35] Zhang, G., J. Li, Y. Chen, H. Xiang, B. Ma, Z. Xu, et al. Encapsulation of copper-based phase change materials for high temperature thermal energy storage. Solar Energy Materials and Solar Cells, Vol. 128, 2014, pp. 131-137.
- [36] Zhou, X., S. Yamashita, M. Kubota, H. Kita. Encapsulated copperbased phase-change materials for high-temperature heat storage. ACS Omega, Vol. 7, 2022, pp. 5442-5452. American Chemical Society.
- [37] Bauer, T., N. Pfleger, N. Breidenbach, M. Eck, D. Laing, and S. Kaesche. Material aspects of Solar Salt for sensible heat storage. Applied Energy, Vol. 111, 2013, pp. 1114-1119.